

# Applied Solid Mechanics Summative Coursework

## Imran Rizki Putranto

### PART A: FINITE ELEMENT ANALYSIS OF A LIFTING LUG

#### INTRODUCTION

Liquefied Natural Gas (LNG) carriers are vessels that move LNG to different locations by transporting them on ships. Throughout its journey, there is a gradual warming of the stored LNG, which causes some of it to boil off. LNG carriers use a Gas Combustion Unit (GCU) to burn the LNG that is boiled off so that only its combustion products are released into the environment rather than the environmentally damaging LNG itself [1].

This report focuses on the stress and deflection analysis of the design of a lifting lug for a GCU. The analysis aimed to justify the proposed design of the lug and ensure that the design is safe enough to lift the GCU by generating and performing finite element analysis (FEA) on Abaqus/CAE [2]. A numerical solution for the stresses and deflection on the lug was found, compared to, and validated against analytical solutions.

#### DESIGN SPECIFICS AND LOADING SCENARIO

The lifting lug, dimensions shown in Figure 1(a) below, was to be made of S355JR structural steel with a uniform thickness of 30mm. Its properties [1] can be seen in Table 1. The GCU, which is roughly cylindrical and weighs 36,000 kg, was to be lifted by six lifting lugs welded to the side of the GCU and spread equally around its circumference [1]. This meant that the load was shared equally between the lugs, resulting in each lug lifting a mass of 6000kg, equivalent to a load of 58,860N. The load experienced by each lug was calculated using Equation 1.

$$F = mg \quad (1)$$

Where F is the load on the lug, m is the mass, and g is the gravitational constant.

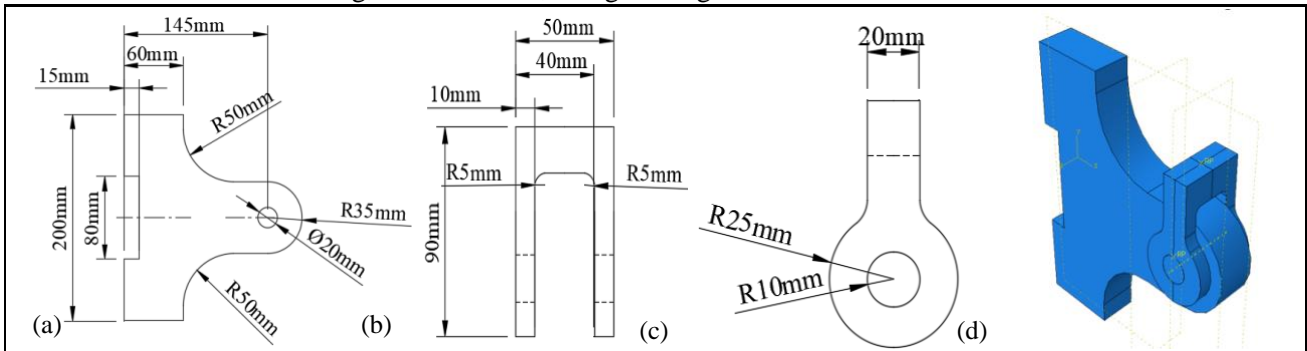


Fig. 1 (a) Dimensions of the lug (b) Front view of shackle, (b) Side view of shackle and (d) Assembly of the Lifting Lug System

Property	Young's Modulus (GPa)	Poisson's Ratio	Yield Strength (MPa)	Ultimate Tensile Strength (MPa)	Elongation at Failure (%)	Density (kg/m <sup>3</sup> )
Value	209	0.3	355	630	22	8010

Table 1 Material Properties of S355JR Structural Steel

A study on the stresses and displacements experienced by the lug during loading was required to ensure that the proposed design can safely lift the GCU without risk of failure. The integrity of the welds was not considered in this study. It was assumed that the GCU would be lifted during ambient environmental conditions without strong winds and that the lifting velocity would be constant.

#### FE MODEL ANALYSIS AND VALIDATION

##### Design and Assembly Methodology

The lug was first modelled on Autodesk Fusion 360 [3]. It was then imported to Abaqus/CAE [2]. A cylindrical pin and a shackle were modelled as rigid bodies due to their arbitrary nature, as their dimensions and material properties were not specified. The pin used was 20mm in diameter and length 50mm. Its clearance with the lug's hole was neglected. The shackle was connected to both ends of the pin, with a 10mm contact length on each side. Its exact dimensions can be seen in Figures 1(b) and (c). The final assembly can be seen in Figure 1(d). Friction at the contact points was modelled with a coefficient of friction of 0.2 [4] for a dry steel – steel contact, assuming that the pin and shackle was also made of steel. Boundary conditions were applied at the

welded side of the lug to restrict all translational degrees of freedom and applied at the top face of the lifting shackle to restrict loading and motion in the X and Z axis since it will be loaded in the Y axis. Since the stresses and deformation of the lifting shackle were not to be considered, the force of 58,860N found above was divided by the cross-sectional area of the top of the lifting shackle (50mm x 20mm). A uniform pressure of 58.86 MPa acting upwards was obtained, assuming that the force was distributed equally on the top of the lug.

### Finite Element Analysis Procedure and Mesh Convergence Study

A mesh convergence study was done for hexahedral, wedge and tetrahedral mesh types with quadratic element orders and starting seed size of 50. A quadratic element order was used instead of linear due to the former utilising a non-linear shape function, and the displacements between the nodes are interpolated using a higher-order polynomial [5]. Quadratic elements are better suited for this analysis as it is better suited to accurately represent complex geometries such as curves and bends, as with this particular model. Meshes with C3D20R hexahedral, C3D15H wedge and C3D10H tetrahedral elements with various seed sizes were done to determine at which seed size each mesh type converges and decide which mesh type is best suited for this geometry. An adaptive mesh was done to refine the elements near bends and curves to produce more accurate results. Unfortunately, this process could only be done for tetrahedral elements, most likely due to their more flexible nature and easier ability to model curves and bends [6]. Despite hexahedral elements generally being the more accurate mesh type [5], the tetrahedral mesh was expected to converge first due to the mesh refinement.

After the stresses and deflection were obtained using the initial seed size, the analysis was repeated using a seed size half of the initial size. The stress error for the second model was calculated using Equation 2 [7].

$$e = \frac{|\sigma_2 - \sigma_1|}{|\sigma_2|} \quad (2)$$

Where  $e$  is the error,  $\sigma_1$  is the stress from the first model and  $\sigma_2$  is the stress for the second model. This process was repeated until a final seed size of 6.25. The final errors obtained for the hexahedral, wedge and tetrahedral elements were 0.0146, 0.0223 and 0.00704, respectively. After four iterations for each mesh type, the tetrahedral mesh type yielded the lowest error and hence seemed to be the best mesh type for this geometry. Several other analyses with different mesh sizes between 6.25 and 50 were then carried out for all three mesh types, and a plot of the mesh convergence study for the maximum stresses outside the contact region and displacements using the three element types are shown in Figure 2(a) and (b) respectively.

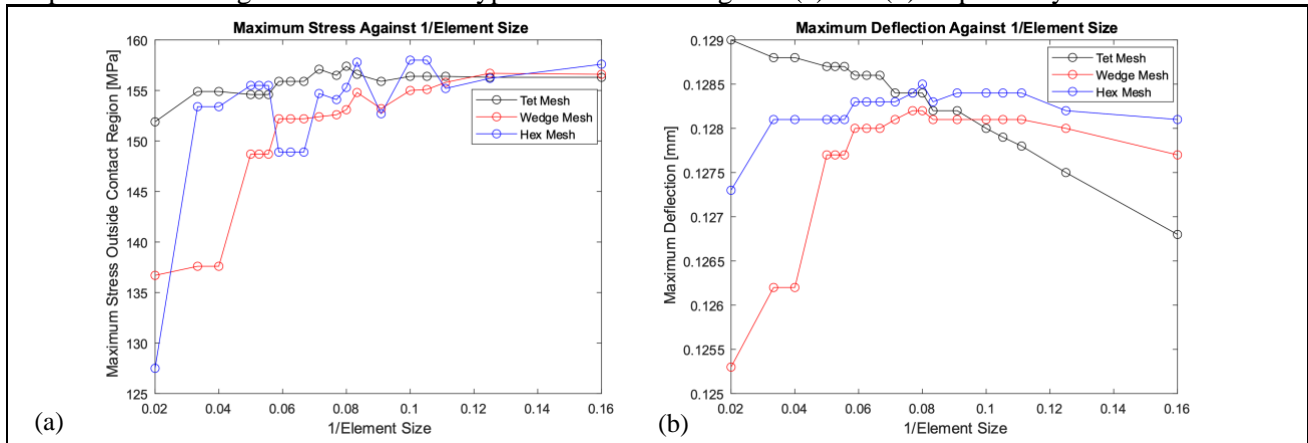


Fig. 2 Mesh Convergence Study for (a) Maximum Stresses Outside the Contact Region in MPa and (b) Maximum Deflection in mm

The tetrahedral mesh type converged fastest when analysing for stresses but did not seem to converge like the hexahedral and wedge mesh types for displacement. However, upon closer inspection of the displacement magnitude, there is only a difference of 0.022mm between the deflections produced by the largest and smallest seed size. Because of the relatively small change in deflection magnitude, convergence was based on the graph for maximum stresses, which in this case, shows that the tetrahedral mesh converges at a seed size of 10 or smaller. Using Equation 2, it was found that there was only a 0.064% error between the stresses produced by a seed size of 10 and the smallest seed size used of 6.25. Plotting a best-fit curve of the results produced by the tetrahedral mesh against the actual data in MATLAB [14] also revealed an RMS error of 0.70977. This was considerably lower than the RMS error of the hexahedral mesh and wedge mesh at 4.6604 and 1.9472, further validating that the tetrahedral mesh was the best element type to use.

## FE Results

The following results were taken from a quadratic tetrahedral mesh with a seed size of 6.25. Figure 3 below shows the results of FE analysis and how stresses and displacements vary along the geometry of the lug. It can be seen that the maximum Von Mises stress outside the contact region is **155.8 MPa** and the maximum overall deflection is **0.1268mm** at the free end. The maximum overall Von Mises stress was found to be 251.2 MPa but repeating the analysis with different seed sizes determined that the stress will never truly converge due to the presence of stress singularities at that point. [8]

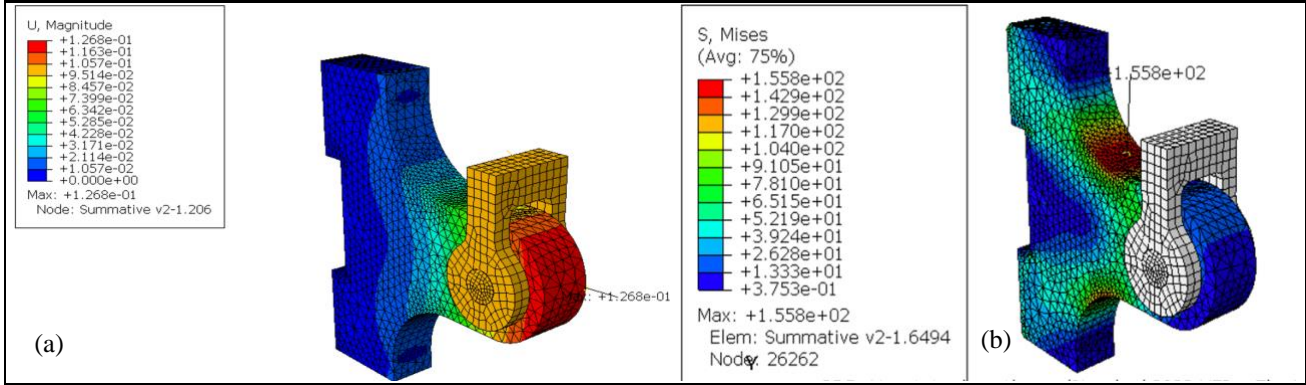


Fig. 3 Results for (a) Maximum displacement in mm (b) Maximum Stress Outside Contact Area in MPa

Element Type and Size	Maximum Stress Outside Contact Region (MPa)	Maximum Displacement (mm)
Quadratic, C3D10H	<b>155.8</b>	<b>0.1268</b>

Table 2 Relevant results from the final mesh used

## ANALYTICAL SOLUTIONS

### Stress

Bearing pressure contact equations were used to determine the contact forces between the pin and the lug due to contact between a convex surface of the former and a concave surface of the latter. Although the pin was modelled as a rigid body, the lug was modelled as an elastic body. The bearing pressure equation for negligible clearance and elastic bodies was used [9] and can be found below.

$$P_{max} = \frac{4}{\pi} \frac{F}{LD} \quad (3)$$

Where  $P_{max}$  is the maximum stress at the contact region,  $F$  is the force applied to the lug,  $L$  is the length of the hole, and  $D$  is the diameter of the hole. This resulted in an analytical maximum reaction pressure of 124.9 MPa at the contact area. This was validated through the maximum S22 stress of 120.3 MPa at the contact area found from the FE analysis. S22 stress was used as this showed the magnitude of the stresses in the y-direction and because the model was constrained to loading and deformation in just the y-direction.

### Deflection

Due to the irregular shape of the lug, some simplifications were done so that an analytical solution could be calculated. The primary assumption was that the lug was approximated to be a short, stubby, simple cantilever beam with a cross-section of 30mm by 70mm. The section of the lug from where the fillet starts until the welded end was ignored and assumed to be a wall to which the beam was attached. Timoshenko Beam Theory was used to determine the maximum deflection of the lug due to its short and stubby nature [**Error! Reference source not found.**]. The equation for the tip deflection with a concentrated end load applied [10] can be seen below:

$$\delta_{tip} = \frac{FL^3}{3EI} + \frac{FL}{kGA} \quad (4)$$

Where  $\delta_{tip}$  is the tip deflection,  $F$  is the force applied,  $L$  is the length of the beam,  $E$  is the Young's modulus,  $I$  is the second moment of area,  $G$  is the shear modulus,  $A$  is the cross-sectional area of the beam and  $k$  is  $\frac{5}{6}$  for a square cross-section beam.

The second moment of area,  $I$ , can be found using Equation 5 [11] below:

$$I = \frac{bh^3}{12} \quad (5)$$

Where  $b$  is the base length and  $h$  is the height of the beam's cross-sectional area. The shear modulus,  $G$ , can be found using Equation 6 [12] below:

$$G = \frac{E}{2(1 + \nu)} \quad (6)$$

Where  $E$  is the Young's modulus and  $\nu$  is the Poisson's ratio of the material.

Since this equation is valid only for a load applied at its end, the beam was assumed to be 85mm in length, such that the load of 58,860N was applied at the end of the beam. The extra horizontal length of 35mm from the arc at the end of the lug was ignored in this case. Using Equation 4 above, a tip deflection of 0.103mm was found. From Figure 3(a) the deflection of the lug at which the load was applied was found to be about 0.1057mm, which is only a 2.62% difference in value. Thus, the results from the FE analysis were most likely valid.

## CONCLUSION

During this study, FE analysis of the proposed lug design was carried out to determine the maximum stress outside the contact region with the pin and the maximum displacement. By varying the mesh sizes of three different mesh types, a tetrahedral mesh element was determined to be best suited for the lug's geometry. Using the results from a quadratic tetrahedral mesh with 6.25 seed size, the maximum stress outside the contact area was found to be 155.8 MPa, and the maximum displacement was 0.1268mm at the free end. Despite having calculated analytical values for maximum contact stress and deflection, these values might not be the most accurate due to some assumptions made during the calculations, as mentioned above. Nevertheless, having these analytical solutions in the same order of magnitude as the FE results indicate that the FE model is most likely valid. The RMS error of the tetrahedral mesh was found to be 0.70977. Typical converged results have a lower magnitudes for the RMS error [13]. Further work could be done to improve the FE model by refining the mesh with smaller seed sizes and consistent step sizes between each seed size to have more confidence in saying that the results have converged, although it will take more time and computing power.

## REFERENCES

1. Velichko, A. & Coules, H., 2022. *Applied Solid Mechanics Assessment Coursework Brief*. Bristol: University of Bristol.
2. Systèmes, D. (1978) "Abaqus/CAE." ABAQUS Inc. Available at: <https://www.3ds.com/products-services/simulia/products/abaqus/abaquscae/> (Accessed: November 14, 2022).
3. Autodesk (2013) "Autodesk Fusion 360." Autodesk. Available at: <https://www.autodesk.com/products/fusion-360/overview?term=1-YEAR&tab=subscription> (Accessed: November 14, 2022).
4. Beardmore, R. (2012) *Friction Factors, Coefficients of friction - Roy Mech*. Available at: [https://roymech.org/Useful\\_Tables/Tribology/co\\_of\\_frict.html](https://roymech.org/Useful_Tables/Tribology/co_of_frict.html) (Accessed: November 14, 2022).
5. *Linear vs Quadratic FE Elements* (no date) *FEA Tips*. Available at: <https://featips.com/2019/03/29/linear-vs-quadratic-fe-elements/> (Accessed: November 21, 2022).
6. Cadence CFD (2022) *Hexahedral Mesh vs Tetrahedral: Comparing High-Quality Meshing*, Cadence - System Analysis. Available at: <https://resources.system-analysis.cadence.com/blog/msa2022-hexahedral-mesh-vs-tetrahedral-comparing-high-quality-meshing> (Accessed: November 21, 2022).
7. Coules, H. (2022) "Finite Element Analysis - Practical Modelling." Bristol: University of Bristol.
8. Skotny, L. (2021) *Stress Singularity - An Honest Discussion*, Enterfea. Available at: <https://enterfea.com/stress-singularity-an-honest-discussion/> (Accessed: November 21, 2022).
9. *Bearing pressure* (no date) *Wikipedia*. Wikimedia Foundation. Available at: [https://en.m.wikipedia.org/wiki/Bearing\\_pressure](https://en.m.wikipedia.org/wiki/Bearing_pressure) (Accessed: November 21, 2022).
10. Dion and Kamran (2021) *Solving Timoshenko Beam Equations for Cantilever Beams*, Engineering Stack Exchange. Available at: <https://engineering.stackexchange.com/questions/48965/solving-timoshenko-beam-equation-for-cantilever-beam> (Accessed: December 1, 2022).
11. Mechanicalc (no date) *Cross section Properties*. Mechanicalc. Available at: <https://mechanicalc.com/reference/cross-sections#:~:text=The%20second%20moment%20of%20area%2C%20more%20commonly%20known,by%3A%20I%20x%20%3D%20E%288%AB%20y%20%20dA> (Accessed: December 1, 2022).
12. *Shear Modulus Formula: Concept, Important Formulas* (no date). Toppr. Available at: <https://www.toppr.com/guides/physics-formulas/shear-modulus-formula/> (Accessed: December 1, 2022).
13. LEAP CFD et al. (no date) *Tips & Tricks: Convergence and Mesh Independence Study*, Computational Fluid Dynamics CFD Blog LEAP Australia New Zealand. Available at: <https://www.computationalfluidynamics.com.au/convergence-and-mesh-independent-study/> (Accessed: December 14, 2022).
14. Moler, C. (1970) "MATLAB," MathWorks. Simulink. Available at: <https://www.mathworks.com/products/matlab.html> (Accessed: November 27, 2022).

## PART B: THEORY OF FEA

This section of the report aims to answer the four questions presented in conjunction with FEA theory. The answers and methodologies to solving them can be found below.

1.
  - a. There are **84 elements** present in the mesh
  - b. There are **56 nodes** present in the mesh
  - c. There are **112 degrees of freedom** present in each mesh. The number of degrees-of-freedom is just twice the number of nodes present, due to the domain being in two dimensions as mentioned in the brief [1].
2. It was mentioned in the brief [1] that the mesh is made up of constant strain triangles. The stiffness matrix for one constant strain triangle element, as asked in the question, can be found using Equation 7 [2] below:

$$K = \iiint_v \mathbf{B}^T(\mathbf{r}) \mathbf{D} \mathbf{B}(\mathbf{r}) dV(\mathbf{r}) = \Delta \mathbf{B}^T \mathbf{D} \mathbf{B} \quad (7)$$

Where:

$\mathbf{B}$  is the matrix given by

$$\mathbf{B} = \frac{1}{2\Delta} \begin{bmatrix} y_2 - y_3 & 0 & y_3 - y_1 & 0 & y_1 - y_2 & 0 \\ 0 & x_3 - x_2 & 0 & x_1 - x_3 & 0 & x_2 - x_1 \\ x_3 - x_2 & y_2 - y_3 & x_1 - x_3 & y_3 - y_1 & x_2 - x_1 & y_1 - y_2 \end{bmatrix}$$

$\Delta$  is given as

$$\Delta = \frac{(x_2 y_3 - x_3 y_2) + (x_3 y_1 - x_1 y_3) + (x_1 y_2 - x_2 y_1)}{2}$$

and  $\mathbf{D}$  for an isotropic material in plane strain is

$$\mathbf{D} = \frac{E}{(1 + \nu)(1 - 2\nu)} \begin{bmatrix} 1 - \nu & \nu & 0 \\ \nu & 1 - \nu & 0 \\ 0 & 0 & \frac{1}{2} - \nu \end{bmatrix}$$

For the terms above,  $E$  is the Young's modulus of 259 GPa,  $\nu$  is the Poisson's ratio of 0.28, and  $x_i$  and  $y_i$  are the coordinates of the node where  $i$  is either node 1, 2 or 3. The coordinates for each node can be seen in Table 3 below:

Node	$x$ coordinate	$y$ coordinate
1	-0.97	0.51
2	0.80	1.13
3	0.03	2.02

Table 3 Coordinates of the nodes of the constant strain triangle element

Using the equations and values above, the stiffness matrix for the constant strain triangle was obtained below:

$$\mathbf{K} = \begin{bmatrix} 0.785 & 0.3838 & -0.8941 & -0.00739 & 0.1092 & -0.3764 \\ 0.3838 & 0.6734 & -0.1453 & 0.2898 & -0.2385 & -0.9632 \\ -0.8941 & -0.1453 & 2.0854 & -0.8457 & -1.1913 & 0.9911 \\ -0.00739 & 0.2898 & -0.8457 & 1.3684 & 0.8531 & -1.6583 \\ 0.1092 & -0.2385 & -1.1913 & 0.8531 & 1.0821 & -0.6146 \\ -0.3764 & -0.9632 & 0.9911 & -1.6583 & -0.6146 & 2.6215 \end{bmatrix} * 10^{11}$$

3. To obtain the magnitude of the reaction forces at Node 2, the equation below was used:

$$\mathbf{f} = \mathbf{K} \mathbf{u} \quad (8)$$

Where  $\mathbf{f}$  is the force matrix acting on the element,  $\mathbf{u}$  is the displacement matrix of the element, and  $\mathbf{K}$  is the stiffness matrix of the element found in question 2. It was given that nodes 2 and 3 are restrained against movement, such that  $u_2$  and  $u_3$  are zero. It is also given the magnitudes of the components of  $f_1$  in the x and y direction are  $158.3 * 10^6$  N/m and  $52.9 * 10^6$  N/m respectively. Note that these forces are normalised with respect to thickness. The resulting elements of the matrices in the equation are seen below:

$$\begin{bmatrix} 158.3 \\ 52.9 \\ f_{2x} \\ f_{2y} \\ f_{3x} \\ f_{3y} \end{bmatrix} * 10^6 = \begin{bmatrix} 0.785 & 0.3838 & -0.8941 & -0.0074 & 0.1092 & -0.3764 \\ 0.3838 & 0.6734 & -0.1453 & 0.2898 & -0.2385 & -0.9632 \\ -0.8941 & -0.1453 & 2.0854 & -0.8457 & -1.1913 & 0.9911 \\ -0.0074 & 0.2898 & -0.8457 & 1.3684 & 0.8531 & -1.6583 \\ 0.1092 & -0.2385 & -1.1913 & 0.8531 & 1.0821 & -0.6146 \\ -0.3764 & -0.9632 & 0.9911 & -1.6583 & -0.6146 & 2.6215 \end{bmatrix} * 10^{11} * \begin{bmatrix} u_{1x} \\ u_{1y} \\ 0 \\ 0 \\ 0 \\ 0 \end{bmatrix}$$

Using the first two rows, a pair of simultaneous linear equations were obtained as seen in below:

$$(0.785 * 10^{11} * u_{1x}) + (0.3838 * 10^{11} * u_{1y}) = 158.3 * 10^6 \quad (9)$$

$$(0.3838 * 10^{11} * u_{1x}) + (0.6734 * 10^{11} * u_{1y}) = 52.9 * 10^6 \quad (10)$$

Solving these two equations for  $u_{1x}$  and  $u_{1y}$  gives a value of  $2.263 * 10^{-3}$  and  $-5.043 * 10^{-4}$  respectively. Putting these two values into the matrix above and taking the third and fourth rows out gives another pair of equations, seen below, which were used to obtain values of  $f_{2x}$  and  $f_{2y}$ , and then used to obtain the magnitude of the reaction force at Node 2.

$$(-0.8941 * 10^{11} * 2.263 * 10^{-3}) + (-0.1453 * 10^{11} * -5.043 * 10^{-4}) = f_{2x} \quad (11)$$

$$(-0.0074 * 10^{11} * 2.263 * 10^{-3}) + (0.2898 * 10^{11} * -5.043 * 10^{-4}) = f_{2y} \quad (12)$$

Solving these two equations, the values of  $f_{2x}$  and  $f_{2y}$  were calculated as -195.007 MN/m and -16.289 MN/m, respectively. To obtain the magnitude of  $f_2$ , the equation below was used:

$$f_2 = \sqrt{(f_{2x})^2 + (f_{2y})^2} \quad (13)$$

A magnitude of **195.69 MN/m** was found for  $f_2$ , per thickness of material.

4. To determine the natural frequency of the system, it is assumed that the system is dynamic and has the equation of motion [3] shown below:

$$\mathbf{f}(t) = \mathbf{M}\ddot{\mathbf{u}}(t) + \mathbf{C}\dot{\mathbf{u}}(t) + \mathbf{K}\mathbf{u}(t) \quad (14)$$

Where  $\mathbf{f}$  is the external forces acting on the system,  $\mathbf{M}$  is the mass matrix,  $\mathbf{C}$  is the damping coefficient matrix,  $\mathbf{K}$  is the stiffness matrix and  $\mathbf{u}$  is the displacement matrix of the system.

Since the natural frequency of the system was to be determined, it meant that there were no external forces acting on the system. Hence,  $\mathbf{f}(t)$  is equal to 0. The material damping was also known to be negligible [1] and thus,  $\mathbf{C}$  is equal to 0. The resulting equation is shown below:

$$\mathbf{M}\ddot{\mathbf{u}}(t) + \mathbf{K}\mathbf{u}(t) = 0 \quad (15)$$

Since the system is linear, all the displacements were assumed to be harmonic in the steady-state solution, such that:

$$\mathbf{u}(t) = \begin{bmatrix} \tilde{u}_1 \\ \tilde{u}_2 \\ \vdots \end{bmatrix} e^{-j\omega t} = \tilde{\mathbf{u}} e^{-j\omega t} \quad (16)$$

Where  $\tilde{u}_1$  and  $\tilde{u}_2$  are complex numbers describing the amplitude and phase of the displacement at each node. Differentiating  $\mathbf{u}(t)$  twice with respect to time gives the acceleration of the system  $\ddot{\mathbf{u}}(t)$ :

$$\ddot{\mathbf{u}}(t) = -\omega^2 \tilde{\mathbf{u}} e^{-j\omega t} \quad (17)$$

Substituting (16) and (17) into (15) and cancelling out  $e^{-j\omega t}$  gives:

$$-\omega^2 \mathbf{M} \tilde{\mathbf{u}} + \mathbf{K} \tilde{\mathbf{u}} = (-\omega^2 \mathbf{M} + \mathbf{K}) \tilde{\mathbf{u}} = 0 \quad (18)$$

The natural frequencies of the system were calculated by equating the determinant of  $(-\omega^2 \mathbf{M} + \mathbf{K})$  to zero as shown below:

$$|\mathbf{K} - \omega^2 \mathbf{M}| = 0 \quad (19)$$

Expanding the terms out forms a polynomial and solving for  $\omega$  gives the natural frequencies of the system.

## REFERENCES

1. Velichko, A. & Coules, H., 2022. *Applied Solid Mechanics Assessment Coursework Brief*. Bristol: University of Bristol.
2. Coules, H. (no date) *Continuum Elements I*. Bristol: University of Bristol.
3. Coules, H. (no date) *Dynamic Analysis*. Bristol: University of Bristol.



## PART C: FAILURE OF MATERIALS

This report section aims to answer two questions in conjunction with the Failure of Materials theory. The answers and methodologies to solving them can be found below. Two separate research investigations related to the structural integrity of service systems on board the LNG carrier were to be completed.

### Question 1: Structural Integrity of a Load-Bearing Component

The first part was to investigate the structural integrity of a load-bearing structural component. The component was made of aluminium, and its material properties can be seen in Table 4 below.

Property	Young's Modulus [GPa]	Poisson's Ratio	Yield Strength [MPa]	Fracture Toughness [MPa√m]
Value	70	0.3	400	20

Table 4 Material Properties of Aluminium

The load-bearing was said to be a large plate with a rectangular cross-section. Because of this, the problem was approached using an infinite plate assumption, such that the geometrical correction factor is approximately equal to one ( $Y \approx 1$ ). It was loaded by two normal stresses  $\sigma_x$  and  $\sigma_y$ , as well as an additional stress  $\sigma_p$  oriented  $30^\circ$  counterclockwise from the positive x-axis with a possible range of  $|\sigma_p| \leq 400$  MPa. It was also assumed that the plate had a central crack at an arbitrary orientation with a minimum detectable crack length,  $2a$ , of 5mm.

Due to the assumption of a large, infinite plate and no stresses being applied in the z-direction, it was assumed that the plate was under plane stress conditions. Therefore, the generalised Hooke's law equations for plane stress [2], was used to determine the minimum number strain measurements needed for this case.

$$\sigma_{xx} = \frac{E}{1 - \nu^2} (\epsilon_{xx} + \nu \epsilon_{yy}) \quad (20)$$

$$\sigma_{yy} = \frac{E}{1 - \nu^2} (\epsilon_{yy} + \nu \epsilon_{xx}) \quad (21)$$

$$\sigma_{xy} = \frac{E}{2(1 + \nu)} \epsilon_{xy} \quad (22)$$

$\sigma_{xx}$ ,  $\sigma_{xy}$  and  $\sigma_{yy}$  are the stress components,  $E$  is the material's Young's modulus,  $\nu$  is the Poisson's ratio, and  $\epsilon_{xx}$ ,  $\epsilon_{xy}$  and  $\epsilon_{yy}$  are the measured strain components. The value of  $\epsilon_{xy}$  was found to be  $-1.0842 \times 10^{-19}$  using the equation below.

$$\epsilon_{xy} = \epsilon_{45} - \left( \frac{\epsilon_{yy} + \epsilon_{xx}}{2} \right) \quad (23)$$

Where  $\epsilon_{45}$  is the strain measured at  $45^\circ$  using the strain gauge.

- As seen above, only **two strain values** are required to obtain both  $\sigma_{xx}$  and  $\sigma_{yy}$ .
- The given MATLAB [3] "fn\_strain" p-code was used to determine the relevant strain values of the plate at  $0^\circ$  and  $90^\circ$ , respectively. This gave the values for  $\epsilon_{xx}$  and  $\epsilon_{yy}$ . Using equations 18 and 19 above, as well as the property values from Table 4, the stresses  $\sigma_{xx}$  and  $\sigma_{yy}$  were found as **-50 MPa and 171 MPa**, respectively.

Due to the sizeable range of applied stress  $\sigma_p$ , it was assumed that the plate could fail by either yielding or fracturing. The two cases were analysed separately and were then used to determine the possible range of  $\sigma_p$  that could be applied to the plate before failing.

### Yielding

To analyse failure by yielding, the principal stresses were required to determine the value of the Tresca and Von Mises yield criteria. The initial stress tensor,  $\bar{\sigma}$ , for the stresses in the x and y directions can be seen below.

$$\bar{\sigma} = \begin{bmatrix} \sigma_{xx} & \sigma_{xy} \\ \sigma_{yx} & \sigma_{yy} \end{bmatrix} \quad (24)$$



Where  $\sigma_{xy}$  is equal to  $\sigma_{yx}$ . Using Equation 22, it was found that  $\sigma_{xy}$  had a negligible value of  $2.919 \times 10^{-15}$  MPa.

The stress tensor was then rotated  $30^\circ$  counterclockwise using Equation 25.

$$\bar{\sigma}' = \mathbf{a} \bar{\sigma} \mathbf{a}^T = \begin{bmatrix} \sigma'_{xx} & \sigma'_{xy} \\ \sigma'_{yx} & \sigma'_{yy} \end{bmatrix} = \begin{bmatrix} \cos \theta & \sin \theta \\ -\sin \theta & \cos \theta \end{bmatrix} \begin{bmatrix} \sigma_{xx} & \sigma_{xy} \\ \sigma_{yx} & \sigma_{yy} \end{bmatrix} \begin{bmatrix} \cos \theta & -\sin \theta \\ \sin \theta & \cos \theta \end{bmatrix} \quad (25)$$

Where  $\sigma'_{xx}$ ,  $\sigma'_{xy}$ ,  $\sigma'_{yx}$  and  $\sigma'_{yy}$  are the new stress components in the rotated coordinate system and  $\mathbf{a}$  is the rotation matrix. This was done so that the magnitude of  $\sigma_p$  could easily be added to  $\sigma'_{xx}$  of the rotated stress tensor, as shown below, due to being aligned at the same axis.

$$\bar{\sigma}' = \begin{bmatrix} \sigma'_{xx} & \sigma'_{xy} \\ \sigma'_{yx} & \sigma'_{yy} \end{bmatrix} + \begin{bmatrix} \sigma_p & 0 \\ 0 & 0 \end{bmatrix} = \begin{bmatrix} \sigma'_{xx} + \sigma_p & \sigma'_{xy} \\ \sigma'_{yx} & \sigma'_{yy} \end{bmatrix} \quad (26)$$

The principal stresses were then found using the equation below and were put in a loop within MATLAB [3] using the range of applied stress  $\sigma_p$ , where  $|\sigma_p| \leq 400$  MPa, giving 801 possible values of  $\sigma_p$  and thus, 801 possible values for the principal stresses  $\sigma_1$  and  $\sigma_2$ .

$$\sigma_{1,2} = \frac{\sigma'_{xx} + \sigma_p + \sigma'_{yy}}{2} \pm \sqrt{\left(\frac{\sigma'_{xx} + \sigma_p - \sigma'_{yy}}{2}\right)^2 + \sigma'_{xy}^2} \quad (27)$$

A graph showing how the principal stresses vary with  $\sigma_p$  is shown in Figure 4 below. From the graph, it is apparent that the principal stresses increase as  $\sigma_p$  increase.

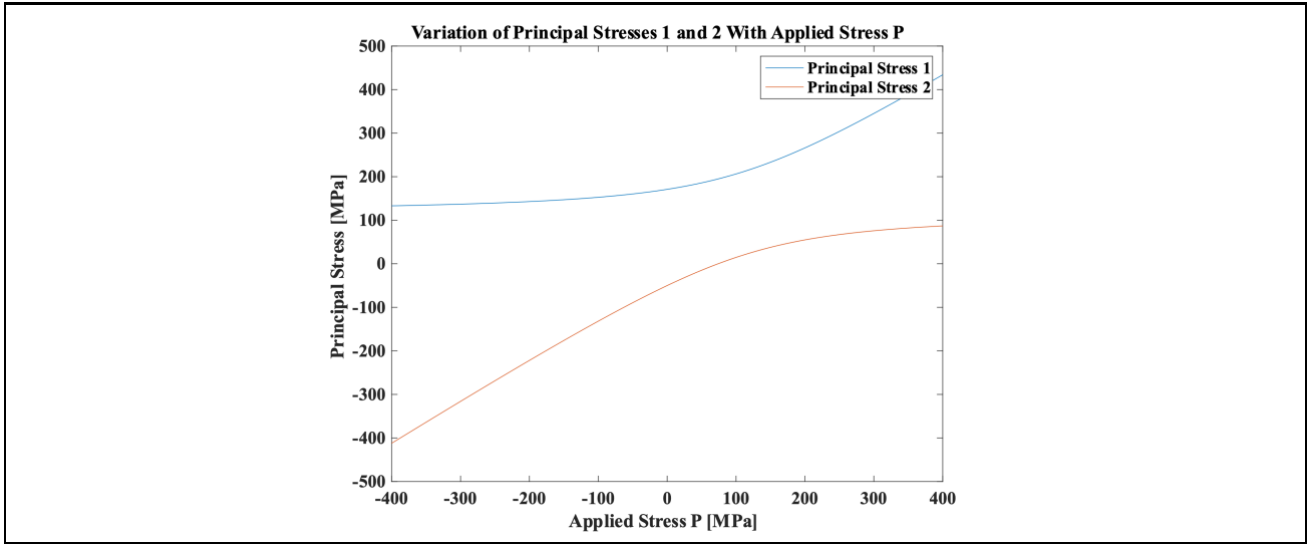


Fig 4. Plot of how Principal Stresses,  $\sigma_1$  and  $\sigma_2$  vary with  $\sigma_p$

The yield criterion for every iteration of the principal stresses was then determined using Tresca and Von Mises yield criteria and was calculated using Equations 28 and 29 [4] respectively.

$$\sigma_{Tresca} = \max(|\sigma_1 - \sigma_2|, |\sigma_2 - \sigma_3|, |\sigma_3 - \sigma_1|) = \max(|\sigma_1 - \sigma_2|, |\sigma_2|, |-\sigma_1|) \quad (28)$$

Where  $\sigma_{Tresca}$  is the Tresca yield criterion for a certain value of principal stresses.

$$\sigma_{VonMises} = \frac{1}{\sqrt{2}} \sqrt{(\sigma_1 - \sigma_2)^2 + (\sigma_2 - \sigma_3)^2 + (\sigma_3 - \sigma_1)^2} = \frac{1}{\sqrt{2}} \sqrt{(\sigma_1 - \sigma_2)^2 + (\sigma_2)^2 + (\sigma_3)^2} \quad (29)$$

Where  $\sigma_{VonMises}$  is the Von Mises yield criterion for a certain value of principal stresses.

A graph showing how the Tresca and Von Mises yield criterion, and their corresponding safety factors varies when the applied stress  $\sigma_p$  was varied are shown in Figures 5(a) and 5(b) below.

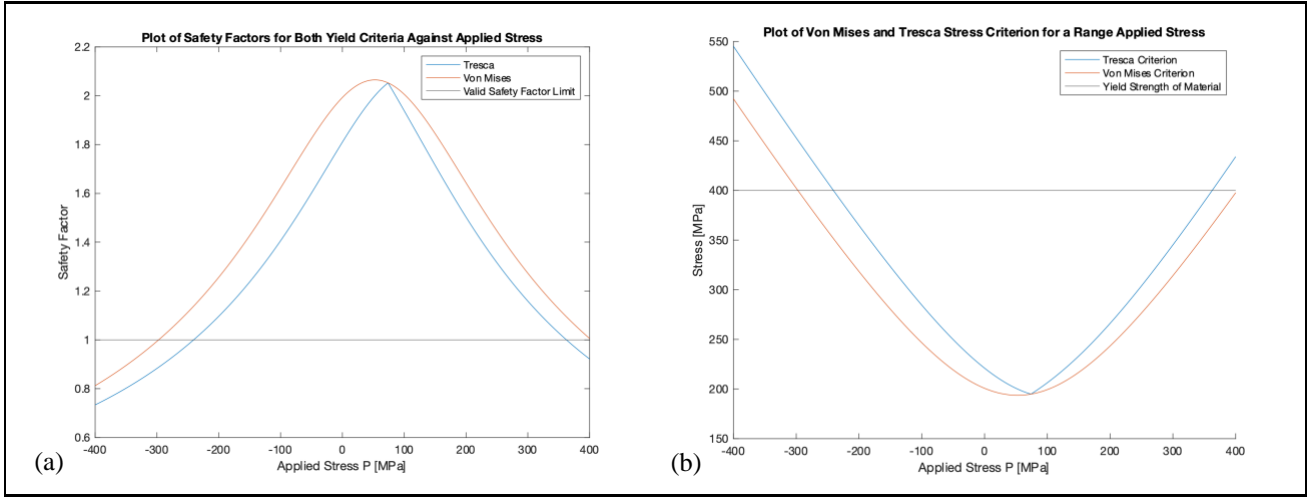


Fig 5. Plot of (a) Safety Factors for Both Yield Criteria and (b) Yield Criteria Values Against Varying Values of  $\sigma_p$

Looking at both figures, it is apparent that the Tresca yield criterion is more conservative due to its smaller range of applicable  $\sigma_p$ . From Figure 5(b), the applicable range of  $\sigma_p$  for Tresca and Von Mises criteria were shown in Table 5 below. The safety factors, seen in Figure 5(a) were calculated using the equation below.

$$SF = \frac{\sigma_y}{\sigma_E} \quad (30)$$

Where  $\sigma_y$  is the material's yield strength and  $\sigma_E$  is the value of the yield criterion. A maximum safety factor of 2.05 and 2.07 were determined from Figure 5(a) using Tresca and Von Mises criterion, respectively. Any value of applied stress  $\sigma_p$  corresponding to a safety factor below 1 was deemed not applicable as the yield criterion value would exceed the material's yield strength of 400 MPa.

	Lower Bound	Upper Bound
Failure Criteria	Applied Stress, $\sigma_p$ [MPa]	Applied Stress, $\sigma_p$ [MPa]
Tresca	- 240	362
Von Mises	- 297	> 400

Table 5 Limits for Tresca and Von Mises Failure Criteria

### Fracture

To analyse failure by fracture, Linear Elastic Fracture Mechanics (LEFM) was first assumed to be valid for all values, meaning that the plastic zone size at the crack tip was negligible. The equation to determine the stress intensity factor for mode I,  $K_I$ , is shown in Equation 31 [5] below.

$$K_I = Y\sigma\sqrt{\pi a} \quad (31)$$

Where  $K_I$  is the stress intensity factor,  $Y$  is the geometrical correction factor,  $\sigma$  is the design stress that propagates the crack growth, and  $a$  is the crack radius or half of the crack length,  $2a$ . Due to a minimum detection size of 5mm [1] for the crack length, an initial value of 2.5mm was assumed for the crack radius,  $a$ . The plate was said to be large with a rectangular cross-section [1]. Hence, it was assumed that the plate has an infinite rectangular cross-section, giving a geometrical correction factor of  $Y \approx 1$ . It was also assumed that the crack is grown through mode I loading, and thus, the design stress used was the stress normal to the crack length, which is always  $\sigma'_{yy}$  of the transformed stress tensor seen in Equation 25.

Due to the arbitrary nature of the crack orientation [1], a MATLAB script was used to loop the equation above for a crack orientation of  $0^\circ$  to  $360^\circ$  at a crack length of 5mm ( $a = 2.5\text{mm}$ ) and the entire range of applied stress  $\sigma_p$  from  $-400$  MPa to  $400$  MPa. To determine the design stress values at each orientation, the stress transformation matrix from Equation 25 was used to rotate the previously rotated stress tensor from Equation 26 with increments of  $1^\circ$ . Using this transformation matrix, the orientation of the x-axis of the transformed coordinate system was assumed to be the crack orientation at that instance. Since the stress tensor being used was already rotated by  $30^\circ$  previously, the starting crack orientation relative to the original coordinate system

was 30°, and it was rotated until it reached 30° again. All plots below start at an angle at 30° and end at 390° to account for the initial 30° rotation. A contour plot showing how the stress intensity factor,  $K_I$ , varies with crack orientation and applied stress  $\sigma_p$  is shown in Figure 6(a) below. Any combination of  $\sigma_p$  and crack orientation that corresponds to a value of  $20 \text{ MPa}\sqrt{\text{m}}$  or greater is not applicable as the material fails by fracture above this point. The areas corresponding to the combinations that are not valid are highlighted in green, as shown in Figure 6(b). From the data, it was determined that the maximum applicable value of  $\sigma_p$  was 137 MPa at a crack orientation of 162°

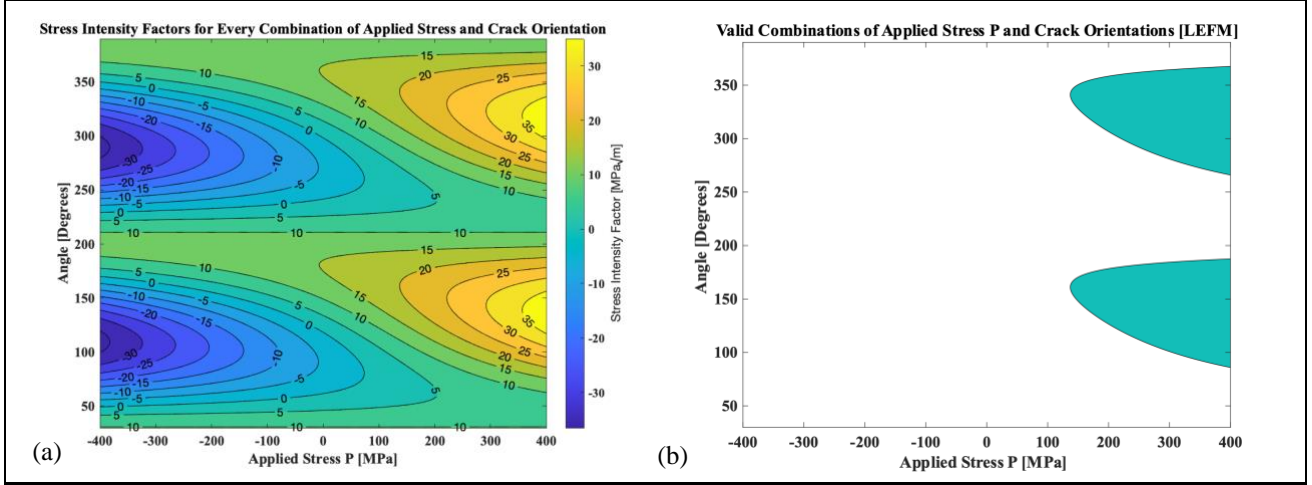


Fig 6. (a) Contour plot of Stress Intensity Factor Values and (b) Applicable Combinations of  $\sigma_p$  and Crack Orientation for LEFM. The LEFM validity equation, seen in Equation 32 [6] below, was then used to determine the validity of LEFM for this scenario.

$$a, (b - a), h \geq \frac{4}{\pi} \left( \frac{K_I}{\sigma_y} \right)^2 \quad (32)$$

Where  $a$  is the crack radius,  $b$  is the plate width,  $h$  is the plate thickness,  $K_I$  is the stress intensity factor from LEFM, and  $\sigma_y$  is the yield strength of the material. Since it was assumed the plate was infinitely long, both  $b$  and  $h$  were assumed to be sufficiently large enough to always be larger than  $a$  and the LEFM validity value. Since  $a$  was initially set to be 2.5mm, the LEFM validity value would have to be equal to or smaller than 2.5mm for LEFM to be a valid assumption for any combination of  $\sigma_p$  and crack orientation. Figure 7(a) shows how the LEFM validity value changes for all values of  $K_I$  calculated according to the different combinations of  $\sigma_p$  and crack orientations and Figure 7(b) shades the combinations which are not valid for LEFM in green.

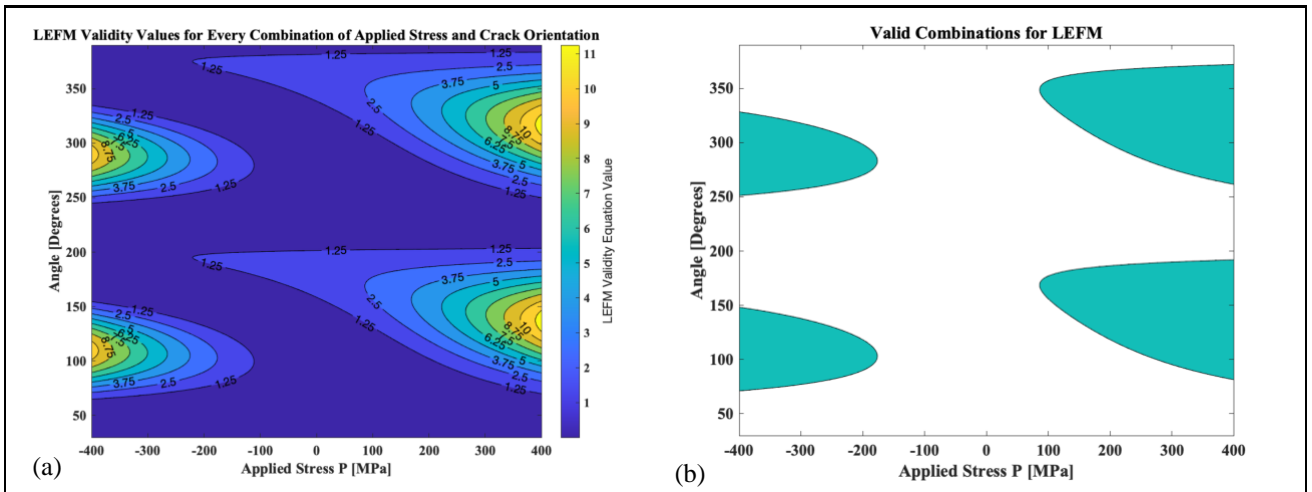


Fig 7. (a) Contour Plot for Variation of LEFM Validity Values and (b) Valid Combinations of  $\sigma_p$  and Crack Orientation for LEFM. As seen in Figure 7(b), a significant minority of combinations produce values that are greater than 2.5mm. This meant that Linear-Elastic Fracture Mechanics is not a valid assumption for these combinations and Elastic Plastic Fracture Mechanics (EPFM) must be used.

To determine the stress intensity factor values when using EPFM, the Irwin correction equation was used, shown by Equation 33 below.

$$K_{eff} = \frac{Y\sigma\sqrt{\pi a}}{\sqrt{1 - \frac{1}{2}\left(\frac{\sigma}{\sigma_y}\right)^2}} \quad (33)$$

Where  $K_{eff}$  is the effective stress intensity factor,  $Y$  is the geometric correction factor  $\approx 1$ ,  $a$  is the crack radius,  $\sigma$  is the design stress, and  $\sigma_y$  is the yield strength of the material. This equation was applied to values which do not satisfy LEFM, while those that do were kept the same.

A new contour plot of how the final stress intensity factor values vary with  $\sigma_p$  and crack orientation can be seen in Figure 8(a).

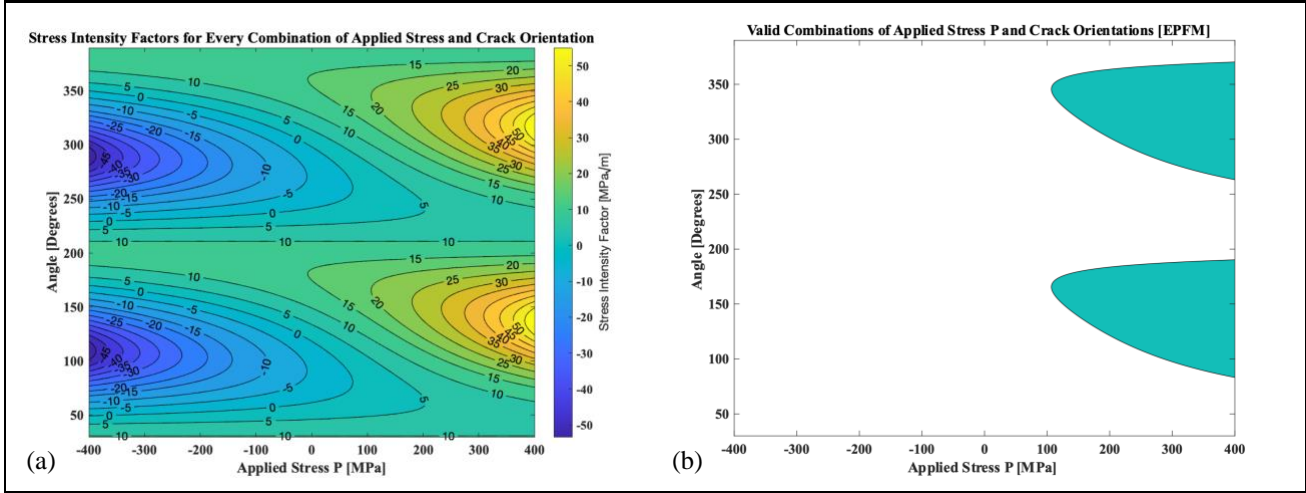


Fig 8. (a) Contour plot of Final Stress Intensity Factor Values and (b) Applicable Combinations of  $\sigma_p$  and Crack Orientations

A plot showing how the stress intensity factors increase as  $\sigma_p$  increases can be seen in Figure 9(a). A polar plot for how the stress intensity factor at the upper limit of  $\sigma_p$  varies according to the crack orientation can be seen in Figure 9(b). From the data, the new maximum applicable  $\sigma_p$  was found to be 106 MPa at a crack orientation of  $166^\circ$  as well as  $346^\circ$  which is just a  $180^\circ$  rotation.

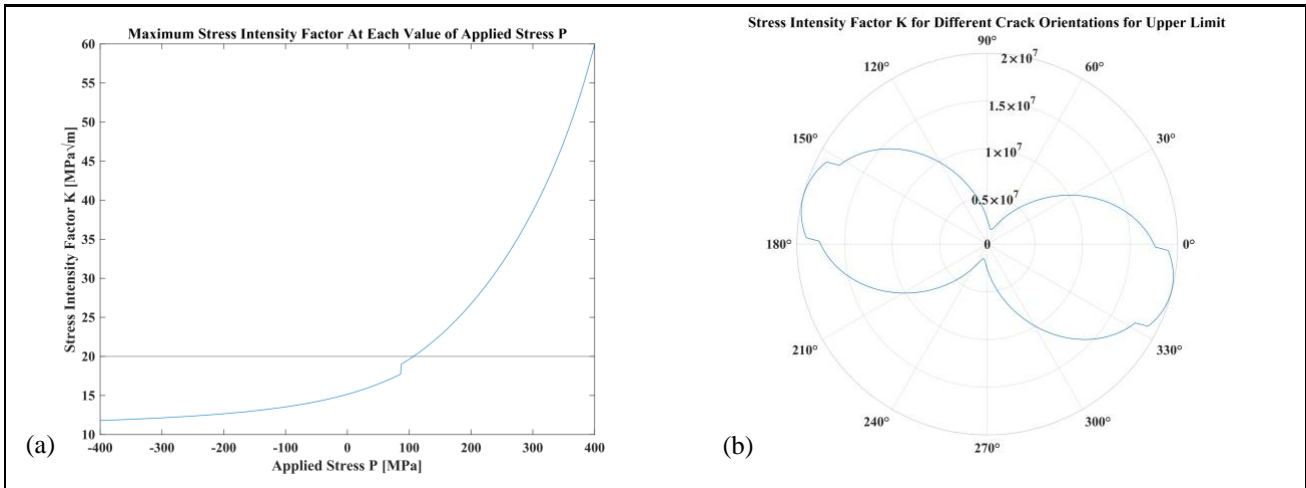


Fig 9. (a) Variation of Stress Intensity Factor Against  $\sigma_p$  and (b) Variation of Stress Intensity Factor Against Crack Orientation

Table 6 below shows the differences in applicable applied stress  $\sigma_p$  as well as the most dangerous crack orientation.

	<b>Maximum Applied Stress, <math>\sigma_p</math> [MPa]</b>	<b>Crack Orientation (<math>^\circ</math>)</b>
<b>LEFM</b>	137	162
<b>EPFM</b>	106	166

Table 6 Limits for Tresca and Von Mises Failure Criteria

- c. From the analysis above, it was determined that the valid range of  $\sigma_p$  such that the material will not fail is  $-240 \text{ MPa} \leq \sigma_p \leq 106 \text{ MPa}$  if accounting for Tresca criterion and  $-292 \text{ MPa} \leq \sigma_p \leq 106 \text{ MPa}$  if accounting for Von Mises criterion. The lower limit was to keep the material from yielding and the upper limit was to keep the material from fracturing. A visual representation of these boundaries can be seen in Figure 10 below. The blue and red boxes highlight the lower and upper bounds for Tresca yield criterion. The Von Mises lower bound, shown in beige, overlaps the Tresca lower bound. The green ellipses show values of  $\sigma_p$  at which the material fractures which varies according to the crack orientation. The most dangerous overall crack orientation is  $166^\circ$  and  $346^\circ$ .

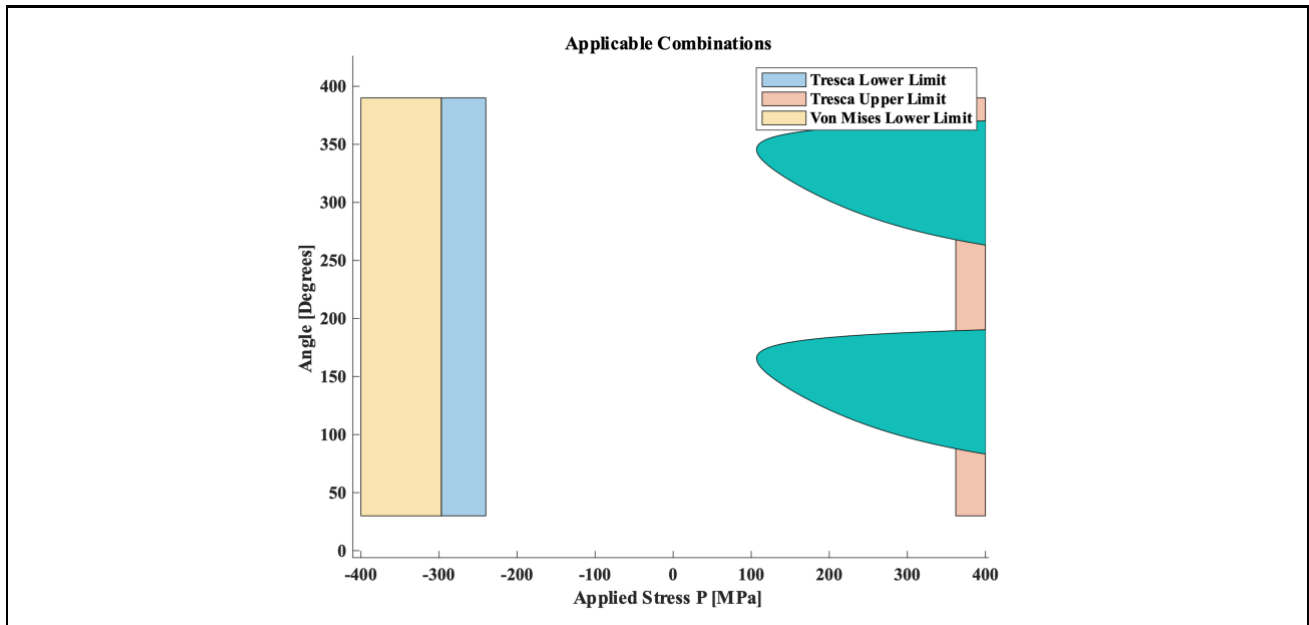


Fig 10. Boundaries for Applicable Values of  $\sigma_p$  and Crack Orientation

### Question 2: Structural Integrity of a Pipe

The second part was to investigate the pipework system's structural integrity of the LNG system. One of the pipework's sections is represented by a steel pipe and undergoes cyclic loading by an internal pressure varying from zero to 40 MPa. Occasionally, there is a possibility of a sudden short-term valve fault, which increases the maximum working pressure to 80 MPa. However, the frequency of these surges is not known [1].

The main task of this part was to determine how the probability of failure of the pipe varies depending on the interval between inspections of the pipe, as well as determining the inspection interval for a probability of failure of 0.01 or 1%. The material properties of the pipe [1], as well as other relevant values, can be seen in Table 7 below. The calculations below were done using the outer diameter of the pipe, but they could also be done with the inner diameter of the pipe.

<b>Property</b>	<b>Outer Diameter, <math>D</math> [mm]</b>	<b>Thickness, <math>t</math> (mm)</b>	<b>Working Pressure [MPa]</b>	<b>Fracture Toughness [MPa<math>\sqrt{m}</math>]</b>	<b>Paris' Law Constant, <math>C</math> [<math>\frac{m/cycle}{MPa\sqrt{m}}</math>]</b>	<b><math>m</math></b>
<b>Value</b>	200	10	40	90	$10^{-12}$	4

Table 7 Material Properties of Steel Pipe and Other Relevant Values

### Probability of Detection as a Function of Crack Length

Firstly, the given MATLAB [3] ‘fn\_pod’ p-code was used to determine the probability that a crack length,  $2a$ , or larger, could be detected. The crack radius,  $a$ , in mm, was used as the input to the p-code. To get an understanding of how a crack’s probability of detection changes when the crack length varies, a plot of the probability of detection against the crack length,  $2a$ , was plotted in Figure 11(a) from an initial crack length of 0.6 mm to 20mm ( $a_i = 0.3\text{mm}$  to  $a_f = 10\text{mm}$ ). An initial crack radius,  $a_i$ , of about 0.1mm to 0.5mm was most commonly assumed for steels [7], and hence, the mean value of 0.3mm was chosen for this assessment. The final crack length of 20mm was chosen as it was assumed that if the crack is semi-circular [1] the pipe will fail by leakage when the radius of the crack,  $a$ , reaches 10mm (crack length,  $2a = 20\text{mm}$ ). This is because the thickness of the pipe is 10mm, and the crack would have propagated 10mm into the thickness of the pipe. However, this assumes the pipe will not fracture before the crack radius reaches 10mm. Due to the nature of the scenario in which LNG is being transported, leakage of the gas from inside the pipe must not occur.

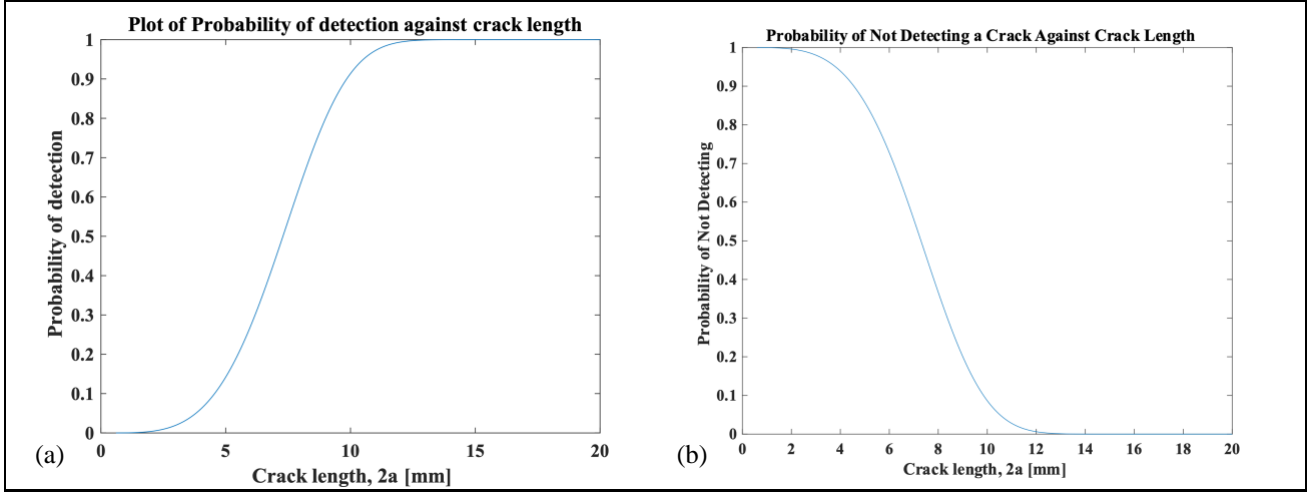


Fig 11. (a) Probability of Detecting a Crack of Length  $2a$  and (b) Probability of Not Detecting a Crack of Length  $2a$

The probability of not detecting a crack at a particular crack length,  $2a$ , or greater for a single inspection can be found using Equation 34 below.

$$P(\text{pod}') = 1 - P(\text{pod}) \quad (34)$$

Where  $P(\text{pod})$  is the probability of detecting a crack of radius  $a$ , and  $P(\text{pod}')$  is the probability that the crack remains undetected. A graph of how  $P(\text{pod}')$  varies when the crack length changes from 0.6mm to 20mm is shown on Figure 11(b).

### Determining the Quickest Failure Mechanism: Fracture or Leakage

According to the brief, the crack grows along the outer wall of the pipe, parallel to the direction of the hoop stress component [1]. The crack depth also propagates into the pipe along its thickness, assuming that crack is semi-circular. The pipe will leak when the radius of crack,  $a$ , reaches 10mm (crack length,  $2a = 20\text{mm}$ ). Considering mode I loading [5], the stress component normal to the crack is the stress that drives the crack growth, which in this case is the axial stress component,  $\sigma_{zz}$ . Its magnitude was found using Equation 35.

$$\sigma_{zz} = \frac{pr}{2t} \quad (35)$$

Where  $\sigma_{zz}$  is the axial stress,  $p$  is the working pressure in the pipe,  $r$  is the pipe outer radius, and  $t$  is the pipe thickness.

The pipe will either fail by leakage or fracture, depending on which happens first. It was mentioned in Table 7 that the pipe has a fracture toughness of  $90 \text{ MPa}\sqrt{\text{m}}$ . For the pipe to fail by fracture instead of leakage, the stress intensity factor,  $K$ , when  $a = 10\text{mm}$ , would need to be greater than its fracture toughness. Equation 31 was used to calculate the stress intensity factor,  $K$ , when the crack radius,  $a$ , was set to 10mm.  $Y$  is a function of crack radius,  $a$ , and is shown in Equation 36 below. A value of 1.072 was obtained for  $Y$  when  $a$  was set to 10mm.

$$Y = 0.728 + 0.373 \left(\frac{a}{t}\right)^2 - 0.029 \left(\frac{a}{t}\right)^4, a \leq t \quad (36)$$



Using the axial stress as the design stress, a stress intensity factor of  $38 \text{ MPa}\sqrt{m}$  and  $76 \text{ MPa}\sqrt{m}$  was calculated for a maximum working pressure of 40 MPa and 80 MPa, respectively. This meant that the pipe would fail by leakage, regardless of whether or not a valve fault occurs.

#### **The Paris Law: Determining the Number of Cycles Until Failure**

The number of cycles it takes to grow a crack from its initial length to its final length was calculated using Equation 37 below, which is derived from the Paris Law, seen in Equation 38.

$$N = \int_{a_i}^{a_f} \frac{1}{C(Y\Delta\sigma\sqrt{\pi a})^m} da \quad (37)$$

Where N is the number of cycles until failure,  $a_i$  is the initial crack radius,  $a_f$  is the crack radius at failure, C and m are Paris Law constants, Y is the geometrical correction factor, and  $\Delta\sigma$  is the difference in the minimum and maximum stresses during cyclic loading. However, since the minimum working pressure is zero,  $\Delta\sigma$  is equal to the maximum axial stress corresponding to the maximum working pressure. Using Equation 37, it was found that about 696,857 cycles were needed to grow a crack from a radius of 0.3mm to 10mm, assuming no valve fault occurs to increase the working pressure to 80 MPa. However, this equation does not show the crack growth rate at each cycle. The Paris Law [8] was used to determine the crack growth rate,  $\frac{da}{dN}$ , during each loading cycle and can be seen in Equation 38 below.

$$\frac{da}{dN} = C(Y\Delta\sigma\sqrt{\pi a})^m \quad (38)$$

MALTAB [3] was used to loop the Paris Law grow a crack from an initial crack radius of 0.3mm to 10mm by iterating Equation 39 below.

$$a_n + \frac{da_n}{dN} = a_{n+1} \quad (39)$$

696,862 iterations were needed for the crack to reach a radius of 10mm, thus validating the previous result of Equation 37 above. A graph showing how the crack length, 2a, increases as the number of cycles increases can be seen in Figure 12(a) below. A logarithmic plot of how the crack growth rate,  $\frac{da}{dN}$ , varies as a function of the stress intensity factor can also be seen in Figure 12(b).

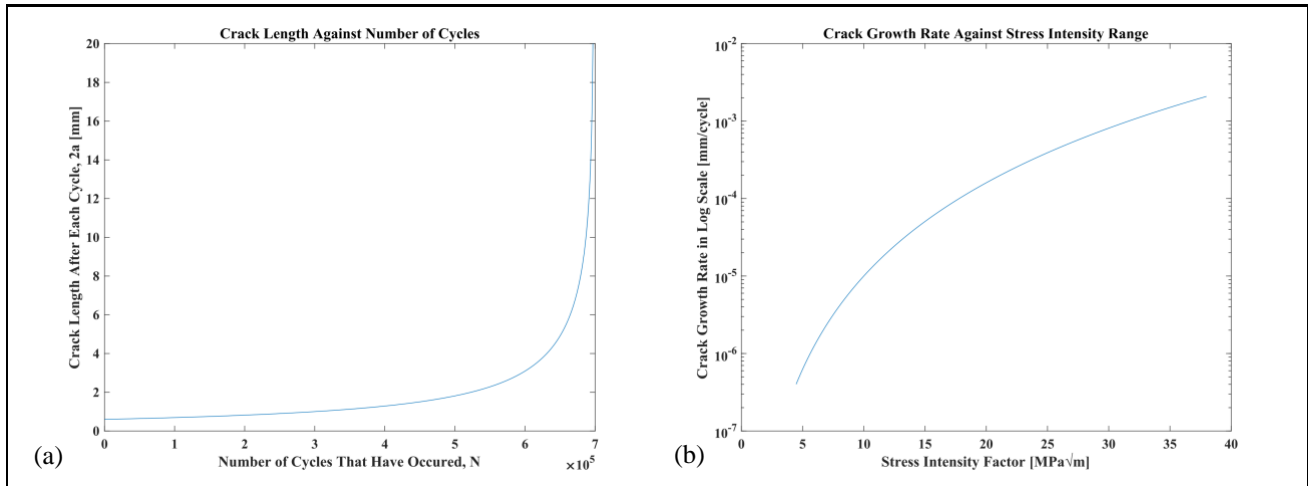


Fig 12. (a) Number of Cycles Until Failure Against Crack Length (b) Crack Growth Rate Against Stress Intensity Factor

#### **The Probability of Failure**

If a single inspection were done at random, the probability that the crack was not detected would depend on the crack length at that instance, as seen in Figure 11(b) above for  $P(\text{pod})$ . However, since there is a possibility for multiple inspections throughout the operating life of the pipe before a crack is detected, the probability of not detecting a crack during each inspection needs to be compounded until either a crack is detected at the final inspection, or the pipe fails, whichever comes first. This is because the pipe can only go through a finite amount of loading cycles until it fails by leakage (i.e. when  $a = 10\text{mm}$ ). Through basic statistics and probabilities, the probability of the crack not being detected at the  $n^{\text{th}}$  inspection, would have to be multiplied by the probabilities at previous inspections, as seen in Equation 40 below.



$$P(det') \Big|_n = P(pod') \Big|_n * P(pod') \Big|_{n-1} \dots * P(pod') \Big|_1 = P(pod') \Big|_n - P(det') \Big|_{n-1} \quad (40)$$

Where  $P(det') \Big|_n$  is the probability of **not** detecting a crack at the  $n^{th}$  inspection and  $P(pod') \Big|_n$  is the probability of **not** detecting a crack of length corresponding to the  $n^{th}$  inspection based on Figure 11(b);  $n = 1, 2, 3, \dots$  until the final inspection. The inspection interval is the number of loading cycles between every inspection. An inspection interval of 100 cycles per inspection corresponds to 100 loading cycles between each inspection.

- a. **The probability of failure is the probability at which a crack is not detected after all possible inspections during the pipe's operating life have been carried out, in which case it fails. The number of possible inspections during the pipe's operating life depends on the interval between the pipe inspections. This shows that the probability of failure depends on the interval between inspections.**

A graph showing how the probability of failure varies when the inspection interval is varied can be seen in Figure 13(a) below, assuming no valve fault occurs. Each circle represents a cycle interval and the probability of failure of the pipe for that specific interval. Each column of vertical scatter plots represents a group of cycle intervals corresponding to a single number of possible inspections. For example, the rightmost vertical column shows a range of cycle intervals between 10,401 and 10,500 cycles per inspection and corresponds to 66 possible inspections during the pipe's operating life. When the total number of cycles until failure is divisible by a specific cycle interval,  $n$ , that cycle interval corresponds to the lowest point of each vertical column. Therefore, it correlates to the lowest probability of failure obtained with the particular number of inspections corresponding to that specific column. The next cycle interval,  $n+1$ , would correspond to the highest point at the next vertical column, which correlates to the subsequent number of inspections.

Figure 13(b) shows the probability of not detecting a crack at each inspection for a cycle interval of 10,401 cycles per inspection, accounting for the compounding probabilities. A total of 66 inspections could be done for this cycle interval, assuming an initial crack radius  $a_i$ , of 0.3mm and a critical crack radius,  $a_f$ , of 10mm. The probability of not detecting a crack at the 66<sup>th</sup> inspection was found to be 0.0019, which is the probability of failure for a cycle interval of 10,401 cycles per inspection.

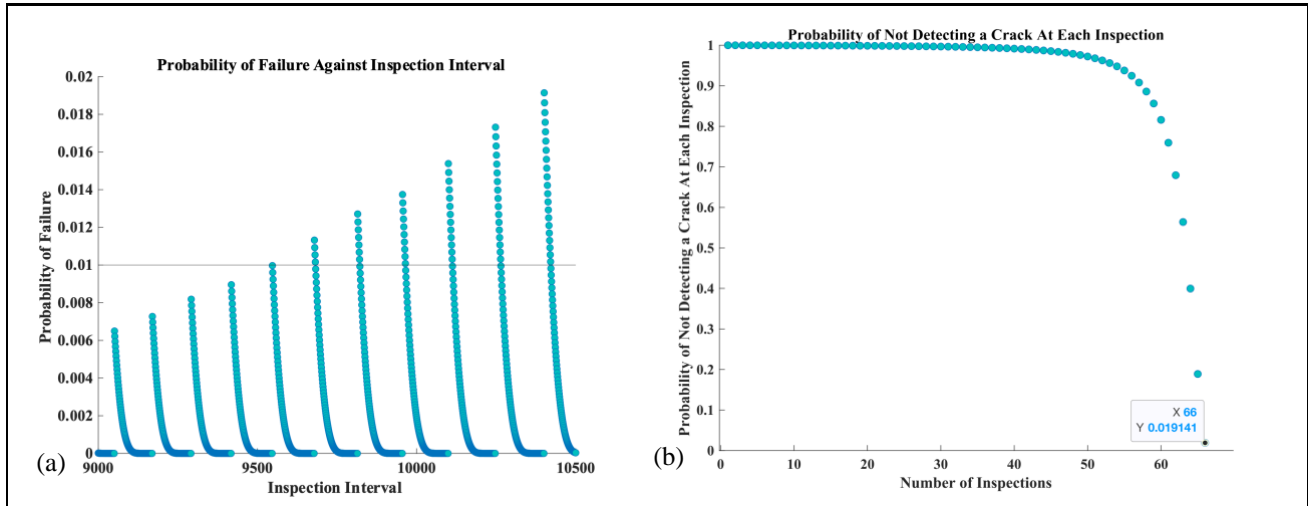


Fig 13. (a) Probability of Failure Against Varying Inspection Intervals and (b) Probability of Not Detecting a Crack at Each Inspection for a Given Inspection Interval

- b. The probability of failure equal to 0.01 corresponds to the probability of not detecting a crack at the final possible inspection being 0.01. Several cycle intervals correspond to a probability of failure of 0.01, shown by the points intersecting the horizontal line in Figure 13(a). Enlarging a section of Figure 13(a) shows that the **minimum cycle interval that gives a probability of failure of 0.01 is between 9682 and 9683 cycles per inspection**, as seen in Figure 14(a) below. Figure 14(b) shows a similar plot to Figure 13(b), but for a cycle interval of 9682 cycles per inspection, **corresponding to 71 possible inspections before the pipe fails.**

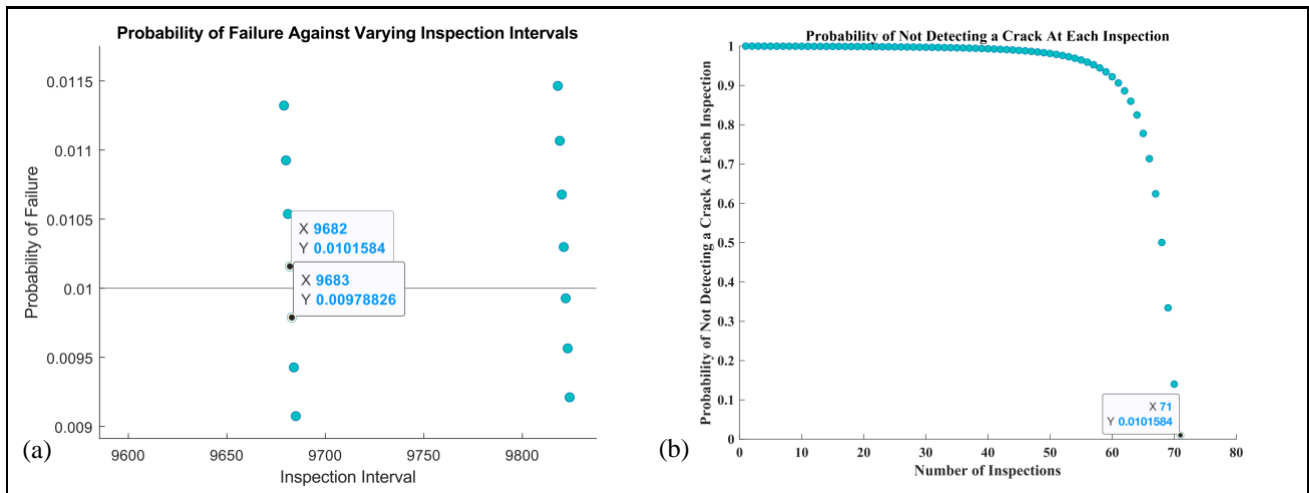


Fig 14. (a) Enlarged Section of Fig 13(a) and (b) Probability of Not Detecting a Crack at Each Inspection for 9682 cycles per inspection

### Accounting for Valve Faults

It was mentioned in the brief that there is a possibility of a valve fault causing a sudden increase in the working pressure to 80MPa. Using Equation 35, the axial stress during a valve fault was 400 MPa. Several assumptions were made to simulate the occurrence of valve faults due to their random nature. The primary assumption was that the valve faults were linearly spaced out. An initial trial was to assume that a valve fault occurs every 100 cycles. Using the Paris Law, it was calculated 605,971 cycles were needed to grow the crack from an initial radius of 0.3mm to 10mm, a difference of 90,891 cycles to if no valve faults occurred. Varying through a cycle interval of 8000 to 8900, it was found that the minimum cycle interval to obtain a probability of failure of 0.01 was between 8301 and 8302 cycles per inspection, corresponding to 72 total possible inspections.

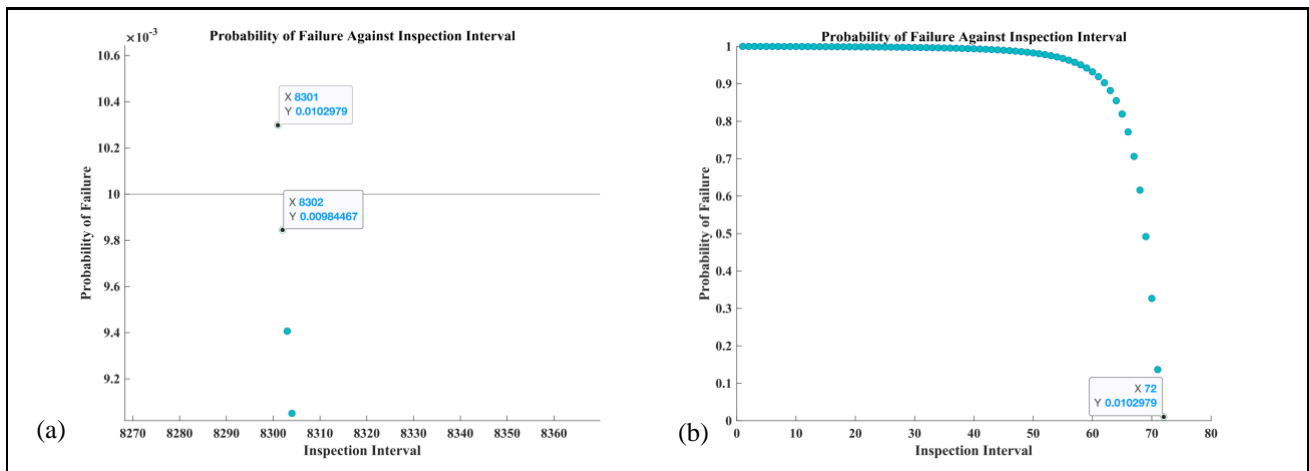


Fig 15. (a) Probabilities of Failure for Equally Spaced Surges and (b) Probability of Not Detecting a Crack at Each Inspection for a cycle interval of 8301 cycles per inspection.

The subsequent trial was to assume that a valve fault occurred at every cycle, effectively making the working pressure 80MPa for all cycles and giving the worst possible scenario. Using the Paris Law once more, only 43,558 cycles were needed to grow the crack from an initial radius of 0.3mm to 10mm, much lower than for a working pressure of 40 MPa. From this, the minimum cycle interval to obtain a probability of failure of 0.01 was about 605 cycles per inspection, shown in Figure 16(a). The probability of not detecting a crack at each inspection can be seen in Figure 16(b). From this figure, a maximum of 71 inspections could be done to obtain a probability of failure equal to 0.01

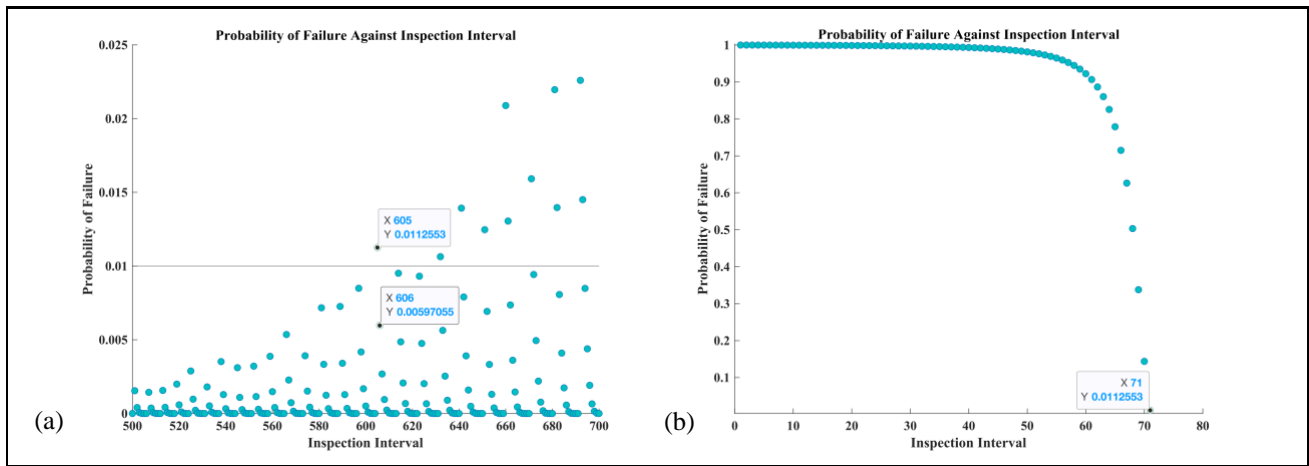


Fig 16. (a) Probabilities of Failures with Varying Inspection Intervals and (b) Probability of Not Detecting a Crack at Each Inspection for a cycle interval of 605 cycles per inspection.

From the three scenarios, it was found that a maximum of about 71 to 72 inspections throughout the entire operating life of the pipe would give a probability of failure equal to 0.01. However, if the frequency of the faults occurring is negligible, it would be safe to assume that the first scenario where no faults occur to be valid. Hence, this would give a cycle interval of about 9682 to 9683 cycles per inspection corresponding to a probability of failure equal to 0.01.

## REFERENCES

1. Velichko, A. & Coules, H., 2022. *Applied Solid Mechanics Assessment Coursework Brief*. Bristol: University of Bristol.
2. *Generalised Hooke's Law* (no date). Missouri University of Science and Technology. Available at: <https://classes.mst.edu/civeng110/concepts/13/hooke/index.html> (Accessed: December 3, 2022).
3. Moler, C. (1970) "MATLAB," *MathWorks*. Simulink. Available at: <https://www.mathworks.com/products/matlab.html> (Accessed: November 27, 2022).
4. Jahed, H. and Roostaei, A.A. (2022) "2 - Fundamentals of cyclic plasticity models," in *Cyclic plasticity of metals: Modeling Fundamentals and Applications*. Amsterdam: Elsevier.
5. Velichko, A. (no date) "Linear Elastic Fracture Mechanics." Bristol: University of Bristol.
6. "Failure of Materials Formula Sheet" (no date). Bristol: University of Bristol.
7. Radaj, D. (1990) "9 - Fracture mechanics approach for assessment of fatigue strength of seam welded joints," in *Design and Analysis of Fatigue Resistant Welded Structures*. Cambridge: Abington Pub., pp. 277–298.
8. Velichko, A. (no date) "Fatigue." Bristol: University of Bristol.